Reconciling tracked atmospheric water flows to close the global freshwater cycle

Reconciling tracked atmospheric water flows to close the global freshwater cycle

Elena De Petrillo
elena.depetrillo@polito.it

Department of Environment, Land and Infrastructure Engineering, Politecnico di Torino, Turin, Italy
https://orcid.org/0000-0001-7398-5742

Simon Fahrländer
Potsdam Institute for Climate Impact Research (PIK), Member of the Leibniz Association, Potsdam, Germany https://orcid.org/0009-0004-8377-530X

Marta Tuninetti
Department of Environment, Land and Infrastructure Engineering, Politecnico di Torino, Turin, Italy

Lauren S. Andersen
Potsdam Institute for Climate Impact Research (PIK), Member of the Leibniz Association, Potsdam, Germany

Luca Monaco
Department of Environment, Land and Infrastructure Engineering, Politecnico di Torino, Turin, Italy; Arpa Piemonte, Turin, Italy

Luca Ridolfi
Department of Environment, Land and Infrastructure Engineering, Politecnico di Torino, Turin, Italy

Francesco Laio
Department of Environment, Land and Infrastructure Engineering, Politecnico di Torino, Turin, Italy

Article

Keywords:

Posted Date: April 30th, 2024

DOI: https://doi.org/10.21203/rs.3.rs-4177311/v1

Additional Declarations: There is **NO** Competing Interest.

Reconciling tracked atmospheric water flows to close the global freshwater cycle

Elena De Petrillo[1*†], Simon Fahrländer[2*†], Marta Tuninetti[1], Lauren S. Andersen[2], Luca Monaco[1,3], Luca Ridolfi[1], Francesco Laio[1]

[1*]Department of Environment, Land and Infrastructure Engineering, Politecnico di Torino, Turin, Italy.
[2]Potsdam Institute for Climate Impact Research (PIK), Member of the Leibniz Association, Potsdam, Germany.
[3]Arpa Piemonte, Turin, Italy.

*Corresponding author(s). E-mail(s): elena.depetrillo@polito.it; simon.fahrlaender@pik-potsdam.de;
Contributing authors: marta.tuninetti@polito.it; andersen@pik-potsdam.de; luca.monaco@polito.it; luca.ridolfi@polito.it; francesco.laio@polito.it;
†These authors contributed equally to this work.

Abstract

Atmospheric moisture plays a vital role in the hydrological cycle, connecting evaporation sources to precipitation sinks. While high-resolution moisture-tracking models offer valuable insight, discrepancies to atmospheric re-analysis data emerge. In this study, we reconcile tracked atmospheric water flows with reanalysis data, using the Iterative Proportional Fitting procedure (IPF). We apply IPF to the atmospheric moisture flows from the UTrack dataset (averaged over 2008-2017), aggregated within countries and ocean boundaries. This reconciled dataset ensures that the total tracked atmospheric moisture equals the total precipitation at the sink and evaporation at the source on an annual basis. Country-scale discrepancies of up to 275% in precipitation and 225% in evaporation are amended, correcting fluxes by $\tilde{0}.07\%$, on average. We find 45% of the total terrestrial precipitation ($\tilde{1}.5 \cdot 10^{\mathbf{5}}$ $\mathrm{km}^{\mathbf{3}}\mathrm{yr}^{\mathbf{-1}}$) originates from land evaporation ($9.8 \cdot 10^{\mathbf{4}}$ $\mathrm{km}^{\mathbf{3}}\mathrm{yr}^{\mathbf{-1}}$). Our reconciled country-scale dataset offers new ground to investigate transboundary atmospheric water flows which connect us globally.

Main

A new view of global freshwater interconnectivity is emerging, where we understand that our collective pressure on the climate and biosphere impacts the stability of the entire global hydrological cycle [1]. Any aspirations for sustainable water stewardship and governance must be based upon an understanding of how hydrological flows interact at local to global scales to shape the global freshwater cycle [2], and how they are affected by cascading effects [3]. Such understanding implies reliable confidence in the estimation of freshwater teleconnections, making it crucial to frame atmospheric moisture flows within the global hydrological cycle. The last decades have seen many improvements in the field of atmospheric moisture tracking and the understanding of region- and country-scale connections. Dirmeyer et al. (2009)[4] were the first to provide a global dataset of country-to-country flows of atmospheric moisture, building on the 3D-QIBT model, based on a quasi-isentropic back-trajectory algorithm [5, 6] forced by reanalysis data at 1.9° and 2.5° resolution [7, 8]. Keys et al. (2017)[9] shed new light on the transboundary governance of water by developing a typology for moisture flow relationships between nations, identifying their characteristics and enabling the classification of different possible governance principles. The work by Link et al.(2020)[10], based on ERA-Interim reanalysis, presented the first grid cell-to-grid cell dataset of moisture flows, with a spatial resolution of 1.5°, including an analysis of the fate of evaporation and the origin of precipitation for several countries. Recently, Tuinenburg et al. (2020)[11] applied the Lagrangian (trajectory-based) tracking model UTrack, which is forced with ERA5 reanalysis data [11], and released a grid cell-to-grid cell dataset [12] of monthly multi-annual means of atmospheric moisture flows (for 2008-2017) from any evaporation source to all its targets (i.e., precipitation) at a spatial resolution of 0.5 degrees with global coverage.

Despite the growing efforts focusing on tracking atmospheric moisture flows, less attention has been given to guarantee the closure of the hydrological balance (i.e. the closure of the hydrological balance for its atmospheric component) on an annual scale and the consistency of the tracked moisture volumes with reanalysis data of precipitation (moisture reaching target cells) and evaporation (moisture departing from source cells).

In this study, we propose a framework to reconcile tracked atmospheric moisture flows, aggregated into a matrix $\mathbf{M}$ of bilateral connections between sources and sinks, with reanalysis data (i.e., a combination of past observations with weather forecasting models to generate consistent time series of multiple climate variables) through the Iterative Proportional Fitting (IPF) approach [13, 14]. The IPF approach is a mathematical method which finds a new matrix $\mathbf{M}_{IPF}$, being the closest to $\mathbf{M}$, but with the row and column totals matching the targeted values.

Here we perform an exemplary case of application of the IPF to the UTrack dataset [12], based on the Lagrangian atmospheric moisture tracking model by Tuinenburg and Staal (2020) [11]. The model tracks single moisture parcels from a column of water vapour at the source in forward direction (from location of evaporation to location of precipitation) until 99% of the original water content of the parcel is precipitated. Running at high spatial and temporal resolution and forced with ERA5 global reanalysis [15], it is currently the state-of-the-art Lagrangian tracking of atmospheric moisture.

The proposed IPF method suits any scale of analysis, from cell to any cell-aggregated scale (e.g., city, country, region, continent). Here, we apply it to a country/ocean scale matrix of flows, aggregated within countries and ocean delineations, and to a sub-continent/ocean matrix, built upon sub-continental regions and ocean classification (see section 3).

Our post-processing framework provides a novel dataset of up-to-date bilateral moisture connections between countries, including oceans, aimed at helping countries manage their portion of the global water cycle. This information enhances the exploration of the role countries and regions play in the international network of atmospheric water flows and the global hydrological cycle, thus supporting global water governance with consistent and reliable data.

The dichotomy between hydrologic reanalysis data and tracked volumes

The UTrack dataset provides for any location c (represented through a cell of 0.5°) a forward footprint matrix (i.e., the fraction of evaporation in c that reaches the downwind cells) and a backward footprint matrix (i.e., the fraction of precipitation in c that comes from evaporation in upwind cells).

Here, we study the annual atmospheric moisture flows at the national level and aggregate the single-cell moisture footprints (both forward and backward) to the country/ocean scale, hence obtaining two matrices of bilateral flows. We consider oceans as sourcing/receiving entities, thus handling them as countries.

The bilateral structure of the country/ocean matrix allows us to evaluate the total precipitation (as imported volume) and total evaporation (as exported volume) of each country/ocean on the average annual scale, on both forward and backward approaches. When comparing the tracked volumes with reanalysis data, a dichotomy between the latter and the tracked volumes arises for both the backward and forward matrices. Specifically, estimated backward volumes result in deviations related to evaporation at the sources (Figure 1a,b), whereas estimated forward volumes are associated with deviations in precipitation at the sinks (Figure 1c,d).

Despite scatter plots suggesting a good correlation between the two data sets, significant percentage deviations both for evaporation (including transpiration over land) ET(from -50% to 225%) and precipitation P (from -50% to 275%) occur at the country/ocean scale. Notably, ET and P deviations at the country/ocean scale are typically out-of-phase, but with different magnitudes of relative deviations: ET overestimation corresponds to P underestimation - e.g., Greenland (+131%, -35%), Russia (+23%, -18%), Ecuador (+24%, -16%) - and *vice versa*, e.g., South Africa (-20%, +50%), Oman (-18%, +92%) and Spain (-15%, +34%). We observe deviations particularly pronounced in regions characterised by aridity – such as countries in Northern Africa, the Middle East, the Arabian Peninsula, and Antarctica – and in the Northern and Southern latitudes. Other relevant differences emerge in Eastern Africa and Southern Europe, where absolute deviations on evaporation in backward tracking are on average -250 $\mathrm{mm} \cdot \mathrm{yr}^{-1}$ (Extended Data Figure 2a). Conversely, in these regions, the absolute deviations in precipitation in forward tracking are on average +600 $\mathrm{mm} \cdot \mathrm{yr}^{-1}$ and +200 $\mathrm{mm} \cdot \mathrm{yr}^{-1}$, respectively (see Extended Data Figure 2b).

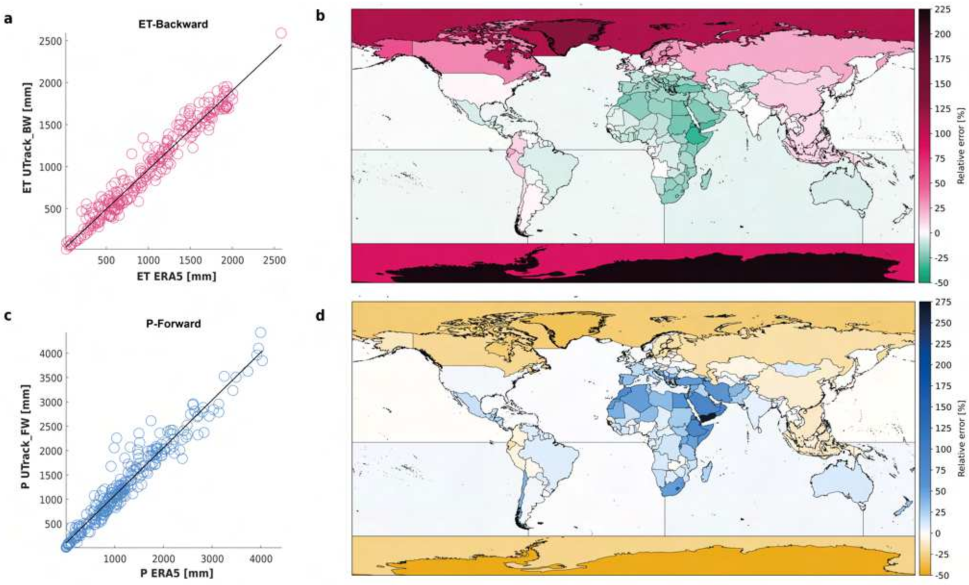

Fig. 1 Deviations between ERA5 data and the UTrack estimates at country/ocean scale. **(a)** Comparison between evaporation estimated by backward approach and ERA5 observations in mm per year, and **(b)** corresponding geography of the relative errors [%]. **(c-d)** The same, but referred to precipitation estimates obtained by forward approach.

A reconciliation framework for atmospheric moisture connections

We solve the dichotomy between country/ocean-scale tracked volumes and the ERA5 re-analysis shown in Figure 1 by adopting the IPF method on both forward and backward matrices. The IPF procedure is a simple and parsimonious methodology that, given a low amount of information – i.e. topology of the network, an initial guess about the entries and the target row and column sums – assures a reliable degree of closeness between the initial and the final adjusted network [16]. Accordingly, we re-scale the elements of the country/ocean matrix of moisture connections, so that the sum of rows and columns in the new matrix meets, respectively, the total precipitation and evaporation data provided by ERA5 at the country/ocean scale. We separately implement the IPF method on the forward flow matrix ($\mathbf{F}$) and backward flow matrix ($\mathbf{B}$) as they are estimated by UTrack, and obtain the IPF-reconciled matrices $\mathbf{F}_{IPF}$ and $\mathbf{B}_{IPF}$. Due to different initial conditions, each single bilateral moisture connection shows a deviation, see Equations 12 – 13 both *ante*-IPF application– with an R^2_{log} of 0.9665 (Extended Data Figure 3a) – and *post*-IPF application despite demonstrating an improved R^2_{log} of 0.9981 (Extended Data Figure 3b). To address the remaining discrepancy between the two bilateral matrices, we average element-wise $\mathbf{F}_{IPF}$ and $\mathbf{B}_{IPF}$ and obtain a unified reconciled matrix $\mathbf{M}_{IPF}$ of moisture connections between countries/oceans.

The new mean matrix $\mathbf{M}_{IPF}$ shows a good correlation with the mean matrix before the IPF application (i.e., $(\mathbf{F}+\mathbf{B})/2$) with an R^2_{log} of 0.997 (Figure 2a). This consistency demonstrates that the IPF algorithm adjusts the bilateral moisture flow matrix to meet ET and P constraints, but does not fundamentally change either the network's topology nor does it significantly impact the largest flows, showing a flow-weighted average difference between the two matrices of 0.067%.

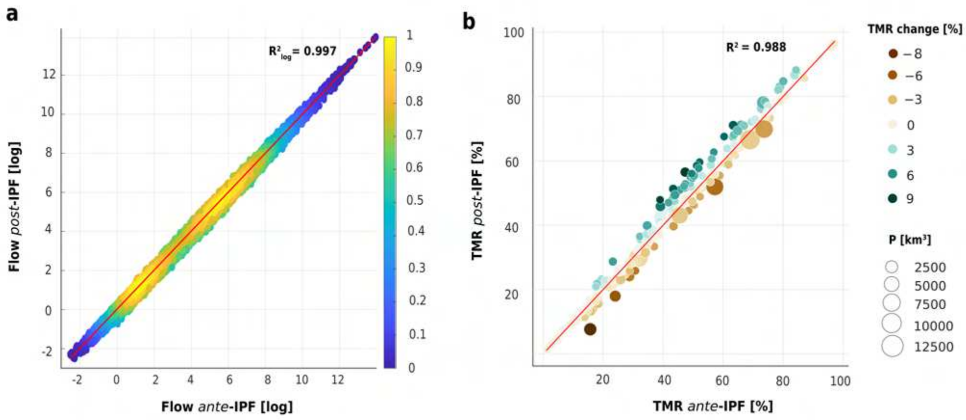

Fig. 2 Comparison of bilateral flow changes *ante*- and *post*-Iterative Proportional Fitting (IPF) application for the composite matrix of forward and backward atmospheric moisture connections sourced from the UTrack dataset and aggregated at the country/ocean scale **(a)** density scatter plot of bilateral moisture volumes before (on the x-axis) and after (on the y-axis) the IPF application (values are plotted in logarithmic scale). **(b)** Scatter plot of the terrestrial moisture recycling (TMR) at the country scale before (on the x-axis) and after (on the y-axis) the IPF application. The circles' size represents the volume of mean annual precipitation (2008-2017), while the circles' colour indicates the relative change [%] of TMR before and after the IPF application.

To evaluate the performance of our reconciliation approach on the network structure, we assess how country-scale terrestrial moisture recycling (TMR)– i.e., the portion of terrestrial precipitation originating from land evaporation– is affected by the IPF application (Figure 2b). On a country scale, Figure 3b shows the TMR relative change after IPF and its spatial heterogeneity worldwide. Notably, the country-specific maximum relative change in TMR does not exceed 9% in absolute values, showing that the global balance of each country-specific network is not heavily affected by the IPF adjustments. The maximum positive relative change (8 to 9%) shown in Figure 3b mainly occurs across countries in East Africa, whereas a maximum relative decrease in TMR is applied to Antarctica (-8%). These adjustments on TMR are not surprising if comparing the relative change in Figure 2 with overestimation of evaporation and underestimation in precipitation shown in Figure 1b and Figure 1d, respectively.
Reconciled country-scale TMR values in Figure 3a also represent valuable information for water and land governance, giving insight into terrestrial evaporation dependencies

and self-resilience of a country for its precipitation. On a global scale, we find an average TMR of 45%, with highest amounts in Mongolia (95%), Central African Republic (CAR) (88%) and Congo (88%), and minimums in Chile (4%, excluding small island nations), see Table 2.

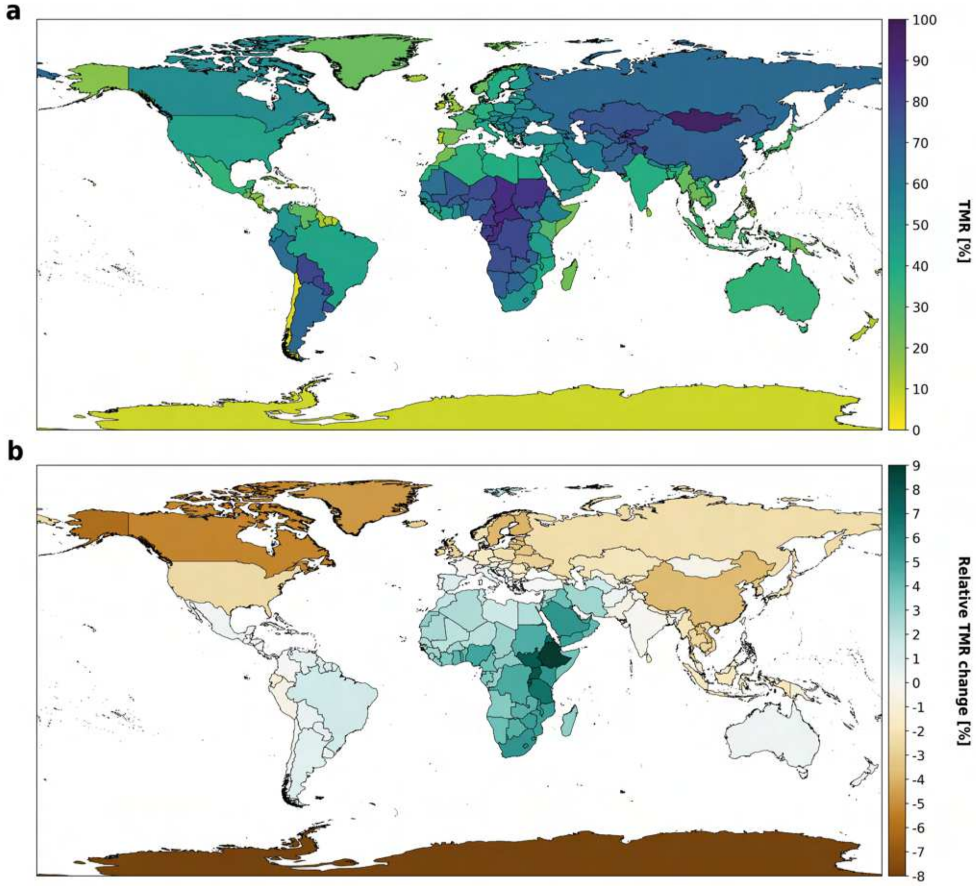

Fig. 3 **(a)** Terrestrial moisture recycling (i.e., precipitation percentage from terrestrial evaporative sources, TMR) obtained at the country scale and **(b)** relative change of TMR [%] at the country scale after the application of IPF.

Balanced bilateral flows at the country scale

In this section, we provide evidence of the importance of post-processing and adjusting the tracked moisture volumes to match ERA5 data for two emblematic examples: South Africa and Brazil. South Africa shows a significant difference between the precipitation and evaporation estimated with UTrack and the ERA5 data (50%, -20%), whereas Brazil represents a well-studied example in the moisture recycling literature and exhibits a UTrack-ERA5 relative error in precipitation and evaporation of just 9% and -6%, respectively.

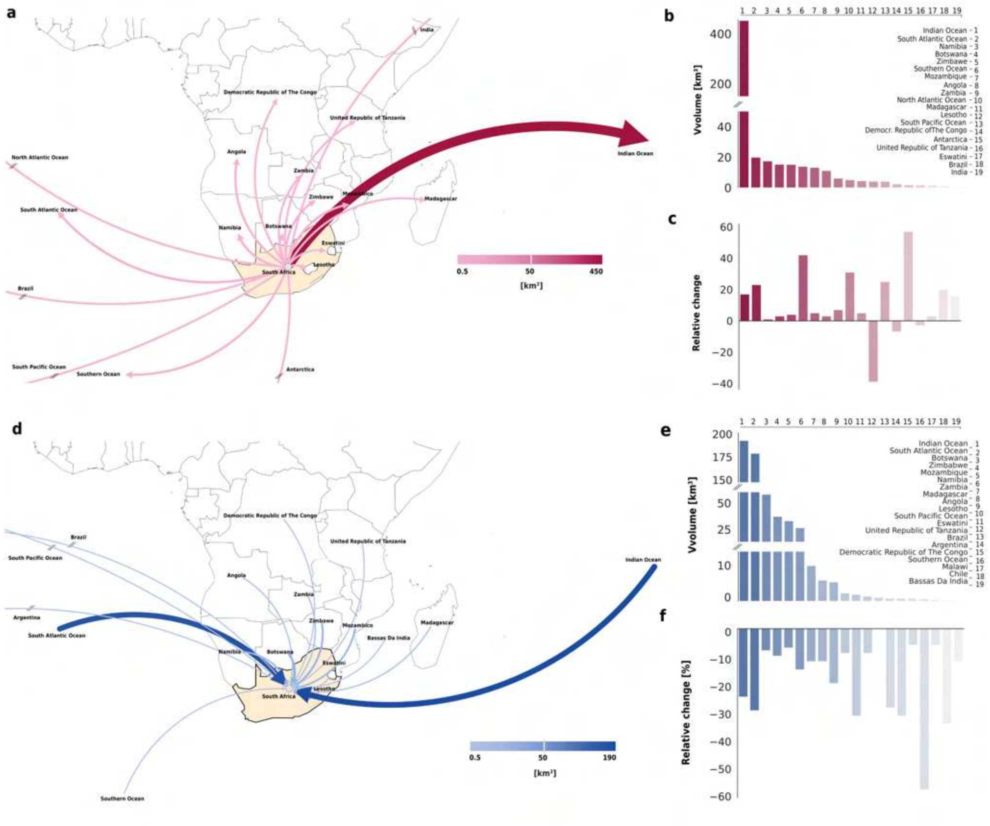

Fig. 4 Major exports (evaporation) **(a)** and imports (precipitation) **(d)** and flows for South Africa after the IPF application. The size of the edges and the colour gradient represent the flows' weight. Panels**(b)** and **(e)** show the resulting volumes of export and import after the IPF reconciliation, respectively. Panels **(c)** and **(f)** report their relative change [%].

While the South African moisture evaporation is strongly directed to the Indian Ocean (453 km^3yr^{-1}), the precipitation sources are more evenly distributed i.e., among the Indian Ocean (190 km^3yr^{-1}), the South Atlantic Ocean (180 km^3yr^{-1}), and several neighbouring countries. 75% of South Africa's total precipitation is sourced by just ten connections, of which 20% originates from terrestrial evaporation from Botswana (58 km^3yr^{-1}), Zimbabwe (38 km^3yr^{-1}), Mozambique (34 km^3yr^{-1}), and Namibia (28 km^3yr^{-1}). *Post*-IPF volumes of precipitation show a monotonous decrease; the major relative changes occur for the Southern Ocean (-59%), Chile (-36%), and the South Pacific (-33%) (Figure 4f) while major evaporation volumes (Figure 4b,c) show an increasing trend, that peaks in Antarctica (+57%) and in the Southern Ocean (+42%).

Despite a former relative error on precipitation and evaporation estimate of 50% and -20%, Africa's key precipitation and evaporation flows are, on average, balanced by small adjustments, by -22% and +16%, respectively.

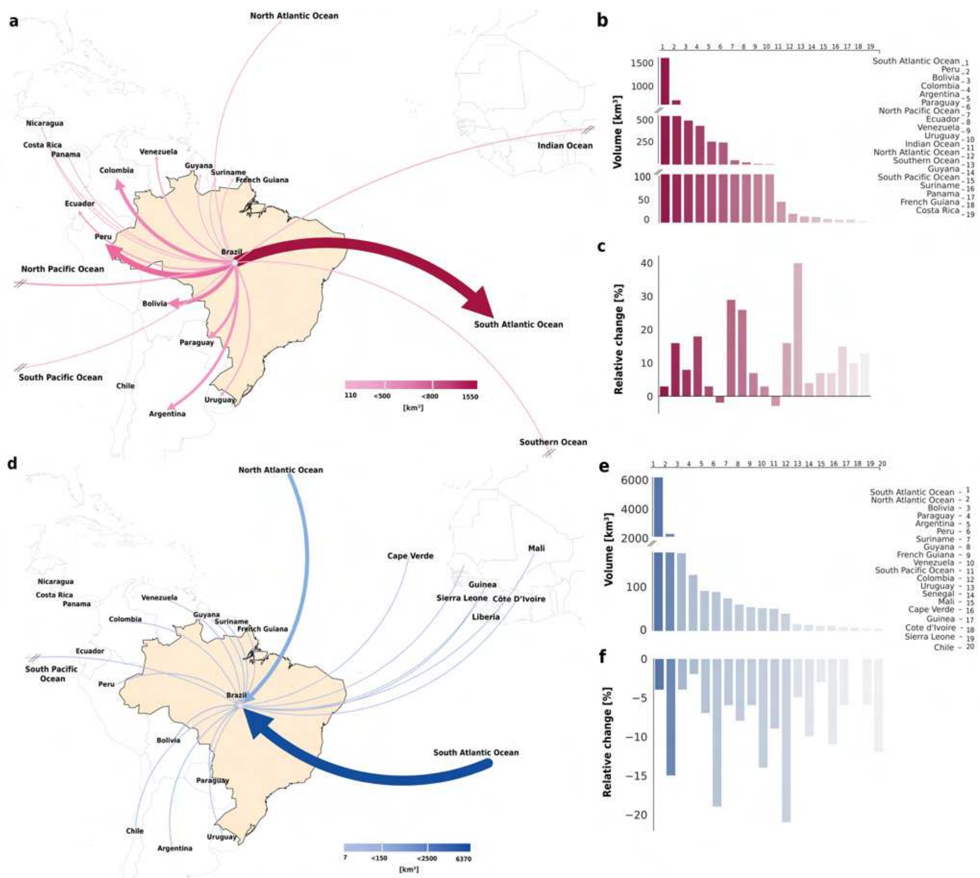

Fig. 5 Major exports (evaporation) **(a)** and imports (precipitation) **(d)** and flows for Brazil after the IPF application. The size of the edges and the colour gradient represent the flows' weight. Panels **(b)** and **(e)** show the resulting volumes of export and import after the IPF reconciliation, respectively. Panels **(c)** and **(f)** report their relative change [%].

In comparison to South Africa, the Brazilian network (Figure 5) shows a narrower adjustment range: relative changes in its major 20 terrestrial connections vary from +39% (Brazil $\rightleftharpoons$ Southern Ocean, 14 km^3yr^{-1}) to -21% (Colombia$\rightleftharpoons$ Brazil, 40 km^3yr^{-1}). Brazil supports the South American regional moisture recycling, which amounts to $1{,}4 \cdot 10^4$ km^3, larger than the strongest bilateral connection between oceans (South Pacific Ocean $\leftrightarrow$ North Pacific Ocean, $1{,}36 \cdot 10^4$ km^3) (Figure 6a), and exports moisture from its rain forest's evaporation downwind to its western neighbours Figure 5a). Its largest annual terrestrial bilateral connections are exports to Peru (780 km^{3}yr^{-1}), Bolivia (510 km^{3}yr^{-1}), and Colombia (460 km^{3}yr^{-1}). These three major flows are changed by 16%, 8% and 18%, respectively, in contrast with the Brazilian export to the Southern Ocean, which reaches about +40% (Figure 5c,e). In general, we observe that in the cases of South Africa and Brazil, the largest relative changes applied by the IPF re-balancing affect flows to the Southern Pole. This behaviour is not surprising, since the polar regions are among the regions mainly affected by precipitation/evaporation errors (Figure 1, Extended Data Figure 2) and consequently adjusted by the reconciliation framework (Figure 3).

Reconciled land and ocean flows of atmospheric moisture at sub-continental scales

The adjusted subcontinental matrix of atmospheric moisture connections, consistent with ERA5 reanalyses (section 3), is shown in the network in Figure 6, divided into terrestrial interactions (panel a) and land-ocean interactions (panel b). Noticeably, the domestically recycled moisture – i.e., the volume of precipitation originating from terrestrial evaporation within the same regional boundaries – of South America and North America (14360 and 6500 km^{3}yr^{-1}, respectively) equals some relevant oceanic connections, e.g. those between the South and North Pacific Ocean (14354 km^{3}yr^{-1}), and between the South Atlantic and the Indian Ocean (5420 km^{3}yr^{-1}).
Zooming in on the terrestrial interactions in Figure 6a, absolute net importing and exporting hubs of terrestrially-sourced mean annual precipitation are highlighted. Among the net importers, Eastern Asia and Eastern Europe are major sinks of net imported precipitation from terrestrial sources (1990 and 1844 km^3 per year, respectively), followed by Western Africa with 1000 km^3. The major ocean$\leftrightarrow$ land flows are the ones from the South and North Atlantic Oceans to South America (8530 and 6360km^3) and from the Indian Ocean to Southeast Asia (6270 km^3), while the largest land $\leftrightarrow$ ocean flows are from South America to the South Atlantic Ocean (3115 km^3), from North America to the North Atlantic Ocean (1940 km^3) and from Eastern Asia to the North Pacific Ocean (1940 km^3), see Figure 6b.
Looking at the domestic moisture recycling (DMR) – measured as domestic precipitation originating from domestic evaporation proportionally to total precipitation in the region– the highest values are exhibited by Central Africa (48%) and South America (44%).

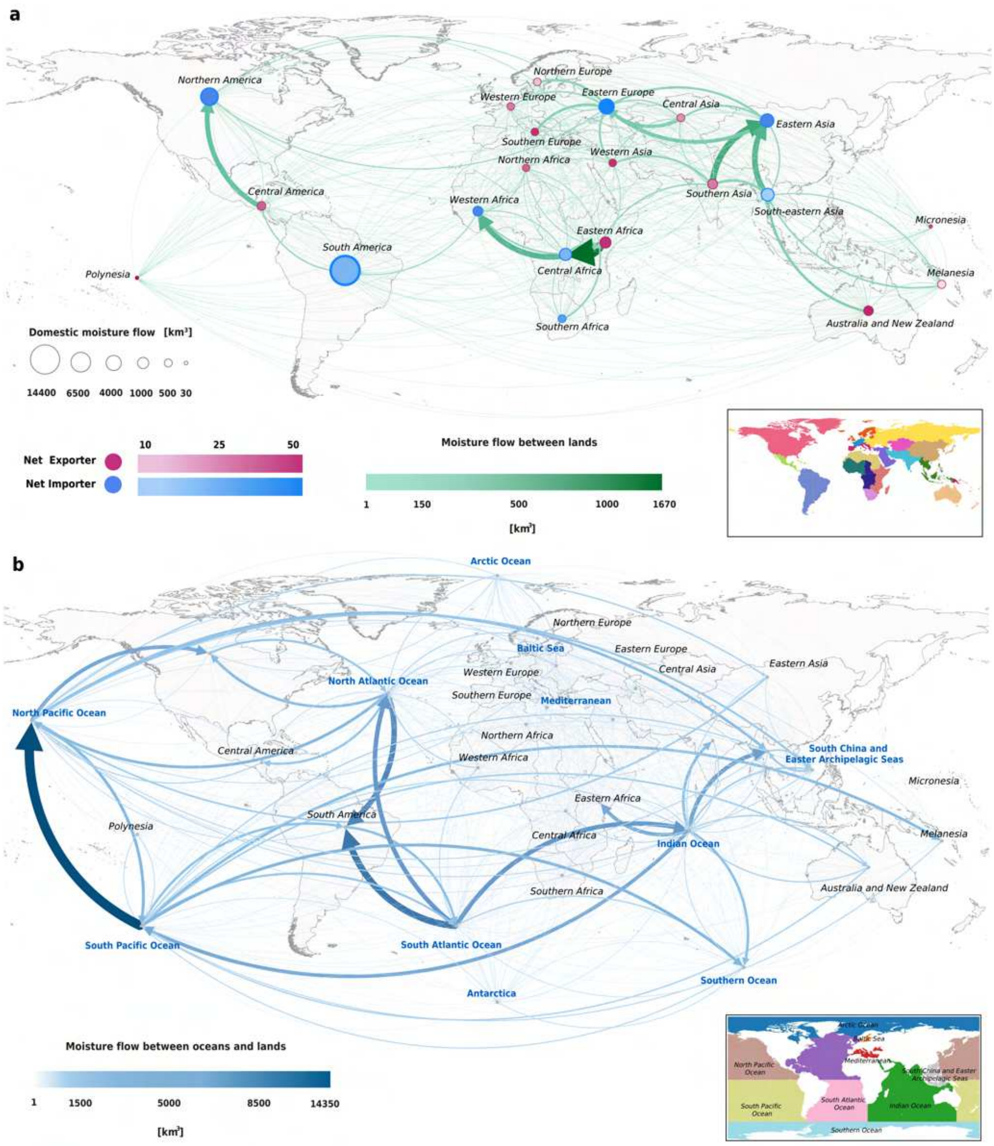

Fig. 6 Moisture connections between subcontinental land regions **(a)** and involving oceans **(b)**. The size and colour of the edges are proportional to the volume evaporated at the source and precipitating at the sink. In panel (a), the node colour indicates if the region is a net importer or exporter of atmospheric moisture from other terrestrial regions, excluding its domestic recycling; their size is proportional to the gross volume domestically recycled i.e., evaporation from the region that precipitates within the region boundaries. Insets show the geographical partitions

Discussion and Conclusion

Atmospheric moisture tracking is a powerful tool to investigate the role of evaporation and precipitation from global to local scales by detecting the source of precipitation. Despite having attracted much attention in the last years, little focus has been put on the consistency of tracked moisture volumes with re-analysis of atmospheric data of precipitation (in target cells) and evaporation (in source cells) nor on guaranteeing internal closure of the moisture balance. This clashes with the awareness that water balance closure is a pivotal factor in hydrological models for strengthening their robustness and enhancing their reliability, especially at global scales [17, 18], and on detecting hydrological changes [19]. The errors we observe (see Figures 1– 2) are recognised by the moisture tracking community; e.g., such deviations are shown in a cell grid map of relative (-) and absolute error ($mm \cdot d^{-1}$) in Tuinenburg et al. (2020)[12]. To fill this gap, we propose the IPF framework to reconcile moisture tracking outcomes with measured (here re-analysed) data. Our IPF approach successfully brings moisture flows to a fitted matrix of bilateral connections which is the closest to the initial one from a topological point of view, but with the total volumes matching the target ones. We here exemplified the capabilities of our approach by referring to UTrack (forward and backward) outcomes and working at annual, country/ocean and sub-continental/ocean scales. We find confirmation of the UTrack atmospheric tracking where IPF applies fewer changes (e.g., Australia, India, Central Europe and South America) while where UTrack shows higher errors in precipitation and evaporation estimates (Northern and Southern poles, oceans and arid regions), IPF introduces significant changes in the total annual water flows (ET and P) in the moisture tracking network.
Estimates in our study shed new light on the global hydrological cycle, closing the annual balance to $5.5 \cdot 10^5$ km^3 per year over the time window from 2008 to 2017, see section 3. From the IPF-balanced matrix of moisture connections, we find that precipitation over land generated from terrestrial and ocean evaporation amounts to $7 \cdot 10^4$ km^3 and $9.3 \cdot 10^4$ km^3 per year, respectively (Table 1). The contribution of terrestrial evaporation to terrestrial precipitation, expressed as TMR, gives useful insights into land resilience, inter-dependencies and vulnerabilities. We find global annual TMR to be 45%, a percentage in between recent findings: van der Ent et al. (2010)[20] report 40% using forward tracking from WAM-2layers model, forced with ERA-Interim data at a 1.5° resolution and Tuinenburg et al. (2020)[12] find 51% using a backward approach in UTrack.

We analysed the quantitative flow dependencies between subcontinents and oceans to ensure the integrity of the global flow network after the IPF reconciliation and then assessed countries as either net importers/exporters of moisture as well as their TMR and DMR ratios. Our country scale hotspots of high TMR in Figure 3a correspond to locations of high-intensity TMR values in grid-based maps presented in previous studies based on the UTrack dataset, such as Tuinenburg et al. (2020)[12] and Posada-Marin et al. (2023)[21]. Net import and net export information on terrestrial flows, as well as TMR and DMR ratios, are useful tools to enhance the applicability of inter-regional land use policies to safeguard atmospheric water flows

Table 1 Global atmospheric water flows from/to land and oceans based on the reconciled atmospheric moisture network. Antarctica is considered together with oceans as one hydrological unit, following Tuinenburg et. al, (2020) [12]

		Oceans	Land
Area	(km^2)	3.6 10^9	1.5 10^9
Precipitation	(km^3 $year^{-1}$)	4 10^5	1.5 10^5
Evaporation	(km^3 $year^{-1}$)	4.5 10^5	9.8 10^4
Precipitation from land evaporation	(km^3 $year^{-1}$)	3.3 10^4	6.53 10^4
Precipitation from ocean evaporation	(km^3 $year^{-1}$)	3.7 10^5	8.3 10^4

as a common, public and transboundary good.
By closing the water balance in a state-of-the-art moisture tracking model output dataset, we offer an example of IPF application to hydrological modelling and take a step towards limiting the inherent uncertainties associated with large-scale moisture flow models and their data inputs.
To evaluate the sensitivity of the IPF method to the scale of application, we analysed the fit of a subcontinent/ocean matrix, aggregated before re-balancing, against a subcontinent/ocean matrix aggregated after a re-balancing applied at the country/ocean scale, as shown in Extended Data Figure 5. We find that the two matrices align well with the one-one line ($R_l^2 log$ equal to 0.9998) and that the the mean deviation between between bilateral flows in the two matrices is 0.084%. This result enforces the general validity of the IPF application and supports further efforts to validate it also including the cell scale of analysis. Given IPF's effectiveness in closing the country scale annual balance while weighting the most affected areas by error, future efforts could be addressed to extend this mathematical approach to finer spatial and temporal scales (e.g., cell scale and month scale).
Though Tuinenburg and Staal (2020) [11] tested the sensitivity of atmospheric moisture recycling to different model assumptions and explicitly show model-dependent uncertainties in estimates across the globe, addressing these limitations, so far, either falls out of scope or goes undetected in UTrack dataset applications (e.g., [22–25]). Further studies can take advantage of our framework to potentially apply it as a post-processing step to reconcile tracked flow (eventually sourced from any other tracking model) with reanalysis data, to any scale of application. In addition, this post-processing approach can help bring more clarity to the uncertainty in and between the different moisture tracking methods, the uncertainty of which still poses an issue for the moisture tracking community, though is currently being addressed through a model intercomparison initiative [26].
Estimates balanced by IPF application, offer a pathway towards a more accurate and reliable understanding of water flows between major geographical and political boundaries, which is crucial for governance, policy and safeguarding of water resources [9, 25, 27–29], showing different insights into the reliance on either terrestrial evaporation from external or internal sources or on oceanic evaporation. Future studies can use our reconciled bilateral network to assess green water resources availability and resilience, and their role in human-ecological systems, delving into the economic importance of green water flows. Enhancing the evaluation of the

amounts of atmospheric moisture across these scales can yield important geopolitical implications by analysing the network globally, and investigating its relation to other socio-hydrological flows, such as the virtual water trade [30].

Methods

Framework

To reconcile the hydrological balance of atmospheric moisture connections — from sources to sinks, considering annual evaporation and precipitation volumes — we employ the Iterative Proportional Fitting (IPF) algorithm. This algorithm operates on the tracked precipitation (forward direction) and evaporation (backward direction) volumes, facilitating adjustments among sources and sinks. This method ensures that the total tracked atmospheric moisture equals the total precipitation at the sink and evaporation at the source on an annual basis.

The proposed approach can be applied to any scale of aggregation (from cell, to countries, regions and continents). In particular, here we chose the country/ocean and subcontinent/ocean scales.

Our framework entails five major steps: (i) Pre-processing and correction of input precipitation and evaporation data to achieve a closed 10-year water balance (Extended Data Figure 1), (ii) Evaluation of forward and backward tracked moisture flows for an average year in the period 2008-2017 as annual imports of precipitation (P) and exports of evaporation (ET) at the country/ocean scale (Figure 1), (iii) Application of the IPF method on the import-export matrices to adjust the discrepancy with ERA5 country/ocean scale data of total annual precipitation and evaporation Figure 2, (iv) Aggregation of country/ocean matrices to subcontinental/ocean scale and IPF application at this scale of analysis, and (v) Validation of the IPF adjustment at the scale of application (Extended Data Figure 5).

Data

The atmospheric moisture connection dataset used in the study is the UTrack dataset [12], available at https://doi.pangaea.de/10.1594/PANGAEA.912710 and accessible through sample scripts provided by the authors. The dataset is based on the Lagrangian atmospheric moisture tracking model UTrack [11].

For each mm of evaporation, the model tracks 100 parcels of moisture throughout the atmosphere from their locations of evaporation to those of precipitation. The tracking is based on ERA5 hourly evaporation and precipitation, wind speed and the three-dimensional wind directions for 25 atmospheric layers in the troposphere at 0.25° horizontal resolution (Copernicus Climate Change Service, C3S) [12]. The moisture tracking runs among all global grid cells including the oceans at 0.25° spatial resolution and consists of three steps: (1) the release of moisture evaporated from the land surface into atmospheric moisture parcels, (2) the calculation of trajectories through the atmosphere for each parcel and (3) the allocation of moisture present in the parcels to precipitation events at the location of the parcel. In addition to the horizontal transport component, the model includes a probabilistic vertical transport scheme that distributes the moisture parcels vertically over 25 atmospheric layers. The parcels are tracked for up to 30 days or until only 1% of the original moisture remains. We refer to the original model development paper by Tuinenburg and Staal (2020)[11] for a more in-depth model description.

The UTrack dataset is available for a reference average year y over the period 2008-2017, on a monthly basis (m) and at grid-cell resolutions of 0.5° and 1°. Here, we source the dataset at a spatial resolution of 0.5°. In the dataset, the selection of a source cell s (location of evaporation) gives a global matrix of the monthly forward footprint, $pf(s,t,m)$ of atmospheric moisture (i.e., the fraction of evaporation from the selected cell s to each target cell t, in the month m) and in reverse, selecting a target cell, t, (location of precipitation) gives the monthly backward footprint of atmospheric moisture, $pb(s,t,m)$ (i.e., the fraction of precipitation in the cell t originating from the upwind evaporation in each source cell s).

Here, we reconstruct the bilateral moisture flows in cubic meters between any sources and sinks using (i) the UTrack monthly forward and backward footprint data of atmospheric moisture connections, i.e., $pf(s,t,m)$ and $pb(s,t,m)$– described above – (ii) the monthly-averaged data of precipitation and evaporation at 0.25° in the cell c for each year y from 2008 to 2017, namely $P_{ERA5}(c,m,y)$ and $ET_{ERA5}(c,m,y)$, expressed in meters per day from the ERA5 Climate Data Store (Copernicus Climate Change Service, C3S), and (iii) the cells areas $a(c)$.
For consistency with the UTrack dataset, available at 0.5° spatial resolution, $P_{ERA5}(c,m,y)$ and $ET_{ERA5}(c,m,y)$ are re-gridded at 0.5° with bilinear interpolation through the CDO operator *remapbil* on a grid [(90,-90),(0,360)].
We calculate the area of the cell grid $a(c)$ through the *gridarea* operator from the Climate Data Operators (CDO) software, a collection of many operators for standard processing of climate and forecast model data [31]. The reference grid to calculate the area of each cell is the input data from the UTrack dataset at the spatial resolution of 0.5°.

ERA5 data pre-processing

The ERA5 dataset is constrained by observations and represents the most detailed available representation of the atmosphere [12]. Hersbach et al. (2020) show that the ERA5 balance between precipitation and evaporation is relatively good for a twenty-year period from the mid-1990s [15], yet the annual balance is not well closed in more recent years. Indeed, Tuinenburg et al. (2020) [12] acknowledge the non-closure between precipitation and evaporation data from the global reanalysis as a source of error in the UTrack dataset itself [12]. To address the non-closure of the hydrological balance, we first analyse the difference between the ERA5 global precipitation and evaporation over the period 2008-2017, namely $P_{ERA5,g}(y)$ and $ET_{ERA5,g}(y)$, calculated as:

$$P_{ERA5,g}(y) = \left[\sum_{c=1}^{N_c} \sum_{m=1}^{12} P_{ERA5}(c,m,y) \cdot a(c) \cdot d(m) \right] \qquad [\mathrm{m^3 yr^{-1}}] \tag{1}$$

$$ET_{ERA5,g}(y) = \left[\sum_{c=1}^{N_c} \sum_{m=1}^{12} ET_{ERA5}(c,m,y) \cdot a(c) \cdot d(m) \right] \qquad [\mathrm{m^3 yr^{-1}}] \tag{2}$$

where N_c is the total number of cells, 720x1440, namely 1'036'800, $a(c)$ the area of the cell and $d(m)$ the number of days in the month m.

Extended Data Figure 1 shows that the annual balance between $P_{ERA5,g}(y)$ and $ET_{ERA5,g}(y)$ is not met along the reference period. Table 1 reports the ratio and the relative error between $P_{ERA5,g}(y)$ and $ET_{ERA5,g}(y)$ for each year of our period of interest. In these ten years of reference, the relative difference between global evaporation estimates and precipitation ranges from -0.4% in 2008 to -1.8% in 2017. The yearly relative difference is evaluated as:

$$\frac{ET_{ERA5,g}(y) - P_{ERA5,g}(y)}{P_{ERA5,g}(y)} \cdot 100 \qquad [\%] \tag{3}$$

Since UTrack data are given as a multi-year average between 2008 and 2017, we calculate the average global volumes of $P_{ERA5,g}(y)$ and $ET_{ERA5,g}(y)$ in the reference period as:

$$P^t_{ERA5,g} = \sum_{y=1}^{10} P_{ERA5,g}(y) \qquad [\mathrm{m^3}] \tag{4}$$

$$ET^t_{ERA5,g} = \sum_{y=1}^{10} ET_{ERA5,g}(y) \qquad [\mathrm{m^3}] \tag{5}$$

where the apex t recalls the time-average over the years 2008-2017.

We impose $P^t_{ERA5,g}$ and $ET^t_{ERA5,g}$ equal their 10-year average (equal to 5.50 $\cdot 10^5$ km^3 yr^{-1}), obtaining the scaling factors α_P and α_{ET} as:

$$\alpha_{ET} = \frac{P^t_{ERA5,g} + ET^t_{ERA5,g}}{2} \cdot \frac{1}{ET^t_{ERA5,g}} \qquad [-] \tag{6}$$

$$\alpha_P = \frac{P^t_{ERA5,g} + ET^t_{ERA5,g}}{2} \cdot \frac{1}{P^t_{ERA5,g}} \qquad [-] \tag{7}$$

Obtaining α_P=0.9971 and α_{ET}=1.0029 Scaling factors are used to re-scale the data of monthly precipitation and evaporation in the year, $P_{ERA5}(c, m, y)$ and $ET_{ERA5}(c, m, y)$ as:

$$P^c_{ERA5}(c, m, y) = \alpha_P \cdot P_{ERA5}(c, m, y) \qquad [\mathrm{m^3yr^{-1}}] \tag{8}$$

$$ET^c_{ERA5}(c, m, y) = \alpha_{ET} \cdot ET_{ERA5}(c, m, y) \qquad [\mathrm{m^3yr^{-1}}] \tag{9}$$

Finally, the corrected yearly volumes $P^c_{ERA5}(c, m, y)$ and $ET^c_{ERA5}(c, m, y)$ are averaged over the number of reference years N_y:

$$\overline{P}^c_{ERA5}(c, m) = \frac{1}{N_y} \cdot \sum_{y=1}^{N_y} P^c_{ERA5}(c, m, y) \qquad [\mathrm{m^3yr^{-1}}] \tag{10}$$

$$\overline{ET}^c_{ERA5}(c, m) = \frac{1}{N_y} \cdot \sum_{y=1}^{N_y} ET^c_{ERA5}(c, m, y) \qquad [\mathrm{m^3yr^{-1}}] \tag{11}$$

UTrack atmospheric moisture flow reconstruction between source and sink cells

We reconstruct annual atmospheric moisture forward and backward flows ($\mathrm{m^3}$) sourcing for each month the forward footprint $pf(s, t, m)$ and the backward footprint $pb(s, t, m)$. Since the footprint of atmospheric moisture is dimensionless and $\overline{ET}^c(c)$ and $\overline{P}^c(c)$ are sourced in meters per day, we consider the area of each cell $a(c)$, as in section 3, in squared meters, and the days in each month $d(m)$ to obtain the cumulated atmospheric moisture volumes in cubic meters. Hereafter the generic cell c is referred to as s when it acts as a source cell, t when it acts as a target cell.
In the forward approach, we evaluate the average annual atmospheric moisture flow, $ff(s, t)$, from a cell s (evaporation) to a matrix of cell t (precipitation) as:

$$ff(s, t) = \sum_{m=1}^{12} \overline{ET}^c(s, m) \cdot pf(s, t, m) \cdot d(m) \cdot a(s) \qquad [\mathrm{m^3yr^{-1}}] \tag{12}$$

In the backward approach, we evaluate the average annual atmospheric moisture flow, $fb_{s,t}$, from a target cell t to a matrix of source cells s as:

$$fb(s, t) = \sum_{m=1}^{12} \overline{P}^c(s, m) \cdot pb(s, t, m) \cdot d(m) \cdot a(t) \qquad [\mathrm{m^3yr^{-1}}] \tag{13}$$

where $pb(s, t, m)$ is previously multiplied for the evaporation of each source cell s, as suggested in Tuinenburg et al., (2020) [12, 32], thus reading:

$$pb(s,t,m) = \overline{ET}^c(s,m) \cdot pb(s,t,m) \qquad [-] \tag{14}$$

Comparing the reconstructed flows in the two cases, we find that a deviation exists, namely:

$$ff_(s,t) \neq fb(s,t) \tag{15}$$

Integration to the country-scale

The spatial scale of this study is primarily set on national boundaries, thus we define a forward matrix **F** and a backward matrix **B** of size $C\times$ C, where C is the total number of countries and oceans (C=272). Each element of the forward (backward) matrix **F** (or **B**) represents the atmospheric moisture flow between an exporting country e and an importing country i, aggregated from the source-sink flows at the cell scale $ff(s,t)$ and $fb(s,t)$ defined in Equation 12 and Equation 13.
However, the conceptual framework and methodologies developed in this research are adaptable and meant to be applied across various scales, ranging from grid cells to other chosen geographical aggregations.
For the geographical delineation of the countries, we access the Administrative Units - Dataset from European Commission Eurostat (ESTAT) GISCO (2020)[33]. Additionally, we choose to include major water bodies (oceans and seas) in the source/target mask to enable a more precise analysis of the oceanic sources of precipitation. The delineations of oceans and seas are taken from the Global Oceans and Seas Dataset of the Flanders Marine Institute (2021)[34] and a delineation of the Caspian Sea from the SeaVoX Salt and Fresh Water Body Gazetteer (v19) of the British Oceanographic Data Centre (2023)[35]. Alterations to the shapefiles, namely the separation of Alaska and Hawaii from the US, the French overseas regions from France and mainland China from Taiwan, are performed in QGIS. Each of the vector shapefiles is rasterized and reformatted into a NetCDF raster masking the geographical delineations with a specific numeric ID for each delineated area using the *gdal_rasterize* and *gdal_translate* operators of the Geospatial Data Abstraction software Library (GDAL)[36]. Subsequently, the three masks are combined while giving priority to the country mask by not overwriting cells with an existing country attribution. Finally, the country-ocean mask is re-gridded using nearest neighbour interpolation through the CDO operator *remapnn* to align with the coordinates of the UTrack dataset.
To allocate each forward and backward flow (i.e., $ff(s,t)$, $fb(s,t)$) to a country/ocean scale bilateral connection in the matrices $F(e,i)$ and $B(e,i)$, we query in both cases if each source cell s falls in the boundaries of e and if the target cell t falls in the boundaries of i, and aggregate the flows as follows:

$$F(e,i) = \sum_{s \in e=1}^{S} \sum_{t \in i=1}^{T} ff(s,t) \qquad [\mathrm{m}^3\mathrm{yr}^{-1}] \tag{16}$$

$$B(e,i) = \sum_{s \in e=1}^{S} \sum_{t \in i=1}^{T} fb(s,t) \qquad [\mathrm{m}^3\mathrm{yr}^{-1}] \tag{17}$$

where S is the total number of source cells located in the country/ocean e and T is the total number of target cells located in the country/ocean i.

The structure of the bilateral matrix, allows us to compare element-wise the reconstructed flows in the two cases. By comparing the bilateral connections element-wise in $F(e,i)$ and $B(e,i)$, we find a deviation with an R^2_{log} of 0.9965 (Extended Data Figure 3a), due to Equation 15.

We also compare the gross precipitation (import) and evaporation (export) flows for each country/ocean both in the forward and backward case. Summing row-wise both $F(e,i)$ and $B(e,i)$ we get the export flow $ET_U(e)$ from the exporting country/ocean e, which represents its annual tracked evaporation the UTrack dataset. Summing column-wise we obtain the import flow $P_U(i)$ of the importing country/ocean i, which represents its annual tracked precipitation from the UTrack dataset. This reads in the forward case:

$$ET^f_U(e) = \sum_{i=1}^{C} F(e,i) \qquad [\mathrm{m}^3\mathrm{yr}^{-1}] \tag{18}$$

$$P^f_U(i) = \sum_{e=1}^{C} F(e,i) \qquad [\mathrm{m}^3\mathrm{yr}^{-1}] \tag{19}$$

and in the backward case:

$$ET^b_U(e) = \sum_{i=1}^{C} B(e,i) \qquad [\mathrm{m}^3\mathrm{yr}^{-1}] \tag{20}$$

$$P^b_U(i) = \sum_{e=1}^{C} B(e,i) \qquad [\mathrm{m}^3\mathrm{yr}^{-1}] \tag{21}$$

Comparing the flows of evaporation $ET^f_U(e)$ and $ET^b_U(e)$ obtained in Equation 18 and Equation 20 we observe that:

$$ET^f_U(i) \neq ET^b_U(i) \qquad [\mathrm{m}^3\mathrm{yr}^{-1}] \tag{22}$$

while comparing the flows of precipitation $P_U^f(e)$ and $P_U^b(e)$ obtained in Equation 19 and Equation 21 we find:

$$P_U^f(i) \neq P_U^b(i) \qquad [\mathrm{m^3 yr^{-1}}] \tag{23}$$

To further understand the nature of this dichotomy, we assess the deviation of the tracked flows at the country/ocean scale $ET_U^f(e)$, $ET_U^b(e)$, $P_U^f(i)$ and $P_U^b(i)$ to ERA5 corrected data on precipitation and evaporation – i.e., $\overline{P}^c_{ERA5}(c,m)$ and $\overline{ET}^c_{ERA5}(c,m)$ (Equation 10, Equation 11). To this aim, we integrate the cell-scale monthly data at the country/ocean and annual scales to obtain $\overline{P}^c_{ERA5,C}(i)$ and $\overline{ET}^c_{ERA5,C}(e)$, that reads

$$\overline{P}^c_{ERA5,C}(i) = \sum_{c\in i=1}^{C}\sum_{m=1}^{12}\overline{P}^c_{ERA5}(c,m) \qquad [\mathrm{m^3 yr^{-1}}] \tag{24}$$

$$\overline{ET}^c_{ERA5,C}(e) = \sum_{c\in e=1}^{C}\sum_{m=1}^{12}\overline{ET}^c_{ERA5}(c,m) \qquad [\mathrm{m^3 yr^{-1}}] \tag{25}$$

Where subscript C recalls country/ocean aggregation.
Comparing Equation 24 with Equation 19 and Equation 21, it emerges:

$$\overline{P}^c_{ERA5}(i) \neq P_U^f(i) \tag{26}$$

Conversely, comparing Equation 25 with Equation 18 and Equation 20:

$$\overline{ET}^c_{ERA5}(e) \neq ET_U^b(e) \tag{27}$$

These deviations are reported in Figure 1.

Iterative Proportional Fitting (IPF) on the country/ocean scale bilateral atmospheric moisture flow matrix

To correct Equation 26 and Equation 27 we separately apply an IPF procedure and bi-proportionally adjust the import-export matrices $\mathbf{F}$ and $\mathbf{B}$, re-scaling the rows and the columns by the minimum amount necessary, to respect the sum constraints $ET_{ERA5}(e)$ and $P_{ERA5}(i)$ until they converge toward a balanced matrix ([13, 16]).

The initial bilateral moisture matrix, $\mathbf{F}$ (or $\mathbf{B}$), is adjusted with two coefficients, a row factor ($r(e)$) and a column factor ($s(i)$), which are obtained with an iterative procedure that progressively updates the initial matrix to obtain the final bilateral moisture matrix, $\mathbf{F}_{IPF}$ (or $\mathbf{B}_{IPF}$), that satisfies the equations

$$\sum_{i=1}^{C} F_{IPF}(e,i) = \overline{ET}^c_{ERA5}(e) \quad \text{and} \quad \sum_{e=1}^{C} F_{IPF}(e,i) = \overline{P}^c_{ERA5}(i) \tag{28}$$

and

$$\sum_{i}^{C} B_{IPF}(e,i) = \overline{ET}^{c}_{ERA5}(e) \quad \text{and} \quad \sum_{e}^{C} B_{IPF}(e,i) = \overline{P}^{c}_{ERA5}(i) \tag{29}$$

The iterative procedure alternatively evaluates the row and the column factors as follows. For example, for the matrix **F**, at step n=1, $s(i)^{n-1}$=1 while $r(e)$ is calculated to satisfy the row constraint, namely

$$r(e)^{n=1} = \frac{\overline{ET}^{c}_{ERA5}(e)}{\sum_{e=i}^{C} s(i)^{n-1} \cdot F(e,i)} \tag{30}$$

At step n=2, $r(e) = r(e)^{n-1}$ and $s(i)$ is equal to

$$s(i)^{n} = \frac{\overline{P}^{c}_{ERA5}(i)}{\sum_{e=1}^{C} r(e)^{n-1} \cdot F(e,i)}. \tag{31}$$

Once the full iteration is completed, it is possible to determine the final row $(R(e))$ and column $(S(i))$ coefficients, namely

$$R(e) = \prod_{n} r(e)^{n} \quad \text{and} \quad S(i) = \prod_{n} s(i)^{n} \tag{32}$$

Hence, the generic adjusted bilateral moisture flow reads

$$F_{IPF}(e,i) = R(e) \cdot F(e,i) \cdot S(i) \quad \text{and} \quad B_{IPF}(e,i) = R(e) \cdot B(e,i) \cdot S(i) \tag{33}$$

Where $R(e)$ and $S(i)$ are matrix-specific and, therefore, they will be different for matrix F and matrix B. At this point, Equation 28 and Equation 29 are satisfied and the dichotomies in Equation 26 and Equation 27 are solved.

The IPF application demonstrates an improved matching between each corresponding bilateral connection in $F_{IPF}(e,i)$ and $B_{IPF}(e,i)$, with R^2_{log} of 0.9981 (Extended Data Figure 3b), especially for larger flows, with respect to *ante*-IPF matrices $F(e,i)$ and $B(e,i)$. However, due to different initial conditions for the bi-proportional fitting, still a weak discrepancy between $F_{IPF}(e,i)$ and $B_{IPF}(e,i)$ remains.

To address the remaining discrepancy between the two bilateral matrices, we evaluate the IPF performance in the two cases, comparing the $F(e,i)$ with $F_{IPF}(e,i)$ and $B(e,i)$ with $B_{IPF}(e,i)$, proving a similar behaviour in the two cases, as shown in Extended Data Figure 3a,b. In light of the similar performance of the IPF application on **F** and **B**, we average element-wise $\mathbf{F}_{IPF}$ and $\mathbf{B}_{IPF}$ and obtain a unified reconciled matrix $\mathbf{M}_{IPF}$ of moisture connections between countries/oceans, as follows:

$$M_{IPF}(e,i) = \frac{F(e,i)_{IPF} + B(e,i)_{IPF}}{2} \tag{34}$$

To compare $M_{IPF}(e,i)$ with *ante*-IPF flows, we perform the same average in Equation 34 also for $F(e,i)$ and $B(e,i)$, obtaining a mean matrix *ante*-IPF application namely $M(e,i)$, as:

$$M(e,i) = \frac{F(e,i) + B(e,i)}{2} \tag{35}$$

The new mean matrix $M_{IPF}(e,i)$ shows a good correlation with the *ante*-IPF matrix $M(e,i)$ (Figure 2a) with R^2_{log} of 0.997.

Integration at the sub-continental scale

Both $\mathbf{F}$ and $\mathbf{B}$ matrices are aggregated to sub-continent/ocean scale matrices $\mathbf{F}^r$ and $\mathbf{B}^r$ and adjusted as in section 3, by separately applying the IPF algorithm on both $\mathbf{F}$ and $\mathbf{B}$ and assess the performance of the application.

The integration to the sub-continental/ocean scale refers for lands to the regions scheme from the United Nation Statistics Division (UNSD, [37]), though with respect to this classification, we aggregate Caribbeans to Central America for consistency of flows in the network. The classification for oceans refers to the Global Oceans and Seas Dataset of the Flanders Marine Institute (2021)[34] and a delineation of the Caspian Sea from the SeaVoX Salt and Fresh Water Body Gazetteer (v19) of the British Oceanographic Data Centre (2023)[35], identically to the country/ocean case analysis (section 3).

To allocate each country/ocean forward and backward flow ($F(e,i)$, $B(e,i)$) to a subcontinent/ocean scale bilateral connection in the matrices $F^r(r_e, r_i)$ and $B^r(r_e, r_i)$, we query in both cases if each exporter country/ocean e falls in the boundaries of the exporter subcontinent/ocean r_e and if the import country/ocean i falls in the boundaries of the importer subcontinent/ocean r_i, and aggregate the flows as follows:

$$F^r(r_e, r_i) = \sum_{e \in r_e = 1}^{R} \sum_{i \in r_i = 1}^{R} \cdot F(e,i) \qquad [\mathrm{m^3 yr^{-1}}] \tag{36}$$

$$B^r(r_e, r_i) = \sum_{e \in r_e = 1}^{R} \sum_{i \in r_i = 1}^{R} \cdot B(e,i) \qquad [\mathrm{m^3 yr^{-1}}] \tag{37}$$

where R is the total number of regions and oceans (equal to 33).

The same aggregation procedure applied to the cell scale ERA5 corrected data in Equations 24 – 25, is here performed to ERA5 country/ocean corrected data for the average year in the period 2008-2017, namely $\overline{P}^c_{ERA5}(i)$ and $\overline{ET}^c_{ERA5}(e)$, as follows:

$$\overline{P}^c_{ERA5,R}(r_i) = \sum_{i \in r_i = 1}^{R} \overline{P}^c_{ERA5}(i) \qquad [\text{m}^3\text{yr}^{-1}] \tag{38}$$

$$\overline{ET}^c_{ERA5,R}(r_e) = \sum_{e \in r_e = 1}^{R} \overline{ET}^c_{ERA5}(e) \qquad [\text{m}^3\text{yr}^{-1}] \tag{39}$$

Where the subscript R recalls the subcontinent/ocean regional aggregation. At this point, the gross import (precipitation) and export (evaporation) are assessed for each subcontinent/ocean element of $\mathbf{F}^r$ and $\mathbf{B}^r$, as follows:

$$ET^f_U(r_e) = \sum_{r_i=1}^{R} F^r(r_e, r_i) \qquad [\text{m}^3\text{yr}^{-1}] \tag{40}$$

$$P^f_U(r_i) = \sum_{r_e=1}^{R} F(r_e, r_i) \qquad [\text{m}^3\text{yr}^{-1}] \tag{41}$$

and:

$$ET^b_U(r_e) = \sum_{r_i=1}^{R} B^r(r_e, r_i) \qquad [\text{m}^3\text{yr}^{-1}] \tag{42}$$

$$P^b_U(r_i) = \sum_{r_e=1}^{R} B(r_e, r_i) \qquad [\text{m}^3\text{yr}^{-1}] \tag{43}$$

Applying IPF to subcontinent/ocean scale bilateral atmospheric moisture flow matrix

The IPF procedure is applied at the subcontinent/ocean scale, following Equations (30), (31), (32), (33), applied to the region/ocean matrices $\mathbf{F}^r$ and $\mathbf{B}^r$.

IPF is applied separately on the two matrices, to get in one case the adjusted $\mathbf{F}^r_{IPF}$ which satisfies equations

$$\sum_{r_i=1}^{R} F^r_{IPF}(r_e, r_i) = \overline{ET}^c_{ERA5}(r_e) \quad \text{and} \quad \sum_{r_e=1}^{R} F^r_{IPF}(r_e, r_i) = \overline{P}^c_{ERA5}(r_i) \tag{44}$$

and in the other case the adjusted $\mathbf{B}^r_{IPF}$, which satisfies equations

$$\sum_{r_i}^{R} B_{IPF}^r(r_e, r_i) = \overline{ET}_{ERA5}^c(r_e) \quad \text{and} \quad \sum_{r_e}^{R} B_{IPF}^r(r_e, r_i) = \overline{P}_{ERA5}^c(r_i) \tag{45}$$

Post-IPF matrices $\mathbf{F}_{IPF}^r$ and $\mathbf{B}_{IPF}^r$ are compared against *ante*-IPF matrices $\mathbf{F}^r$ and $\mathbf{B}^r$, to assess the changes brought by the IPF to the network at this scale of analysis. Panels c and d in Extended Data Figure 3 show that also at the subcontinent/ocean scale, the IPF works likewise in the forward and backward cases. In light of this result, we calculate the mean matrix $\mathbf{M}^r$ *ante*-IPF and $\mathbf{M}_{IPF}^r$ *post*-IPF, as in Equations (35) and (34). Results shown in Figure 6 refer to the adjusted mean matrix $\mathbf{M}_{IPF}^r$.

Inter-scale validation

The subcontinental scale analysis also serves as a validation procedure to evaluate the sensitivity of the IPF method to the scale of application. To this aim, we aggregate the *post*-IPF country/ocean matrix $\mathbf{M}_{IPF}$, at a subcontinent/ocean scale matrix, $\mathbf{M}_{IPF}^{aggr,r}$, and analyse its fit with the adjusted subcontinental-ocean matrix $\mathbf{M}_{IPF}^r$ obtained in the previous section (see Equations 44 –45).
The subcontinent/ocean matrix $\mathbf{M}_{IPF}^{aggr,r}$ is aggregated from the adjusted country/ocean matrix $\mathbf{M}_{IPF}$ as follows:

$$M_{IPF}^{r,post}(r_e, r_i) = \sum_{e \in r_e = 1}^{R} \sum_{i \in r_i = 1}^{R} \cdot M_{IPF}(e, i) \qquad [\mathrm{m^3 yr^{-1}}] \tag{46}$$

Matrices $\mathbf{M}_{IPF}^r$ and $\mathbf{M}_{IPF}^{aggr,r}$ are compared element-wise as:

$$\epsilon(r_i, r_e) = \frac{M_{IPF}^r(r_i, r_e) - M_{IPF}^{r,post}(r_i, r_e)}{M_{IPF}^r(r_i, r_e)} \qquad [-] \tag{47}$$

The mean relative deviation reads

$$\bar{\epsilon} = \frac{\sum_{r_i=1} \sum_{r_e=1}^{R} \epsilon_{rel}(r_i, r_e)}{\sum_{r=1}^{R} M_{IPF}^r(r_i, r_e)} \cdot 100 \qquad [\%] \tag{48}$$

and gives $\bar{\epsilon}$=0.084%.
Estimates of bilateral flows in $\mathbf{M}_{IPF}^r$ and $\mathbf{M}_{IPF}^{aggr,r}$ are plotted against each other in Extended Data Figure 5.

Data availability

All the input data used in this study are taken from publicly available sources.

The dataset generated in the current study is available at 10.5281/zenodo.10400695.

Code availability

The codes developed for the building and processing of the data are available on GitHub at https://github.com/elenadepetrillo/atmospheric_moisture_matrix.

Author contributions

E.D.P., S.F., M.T., L.S.A., L.R., and F.L. conceived the study. E.D.P., S.F, M.T., L.M., performed the analyses and E.D.P. and S.F. produced the figures. All authors contributed to data interpretation. E.D.P., S.F., M.T., L.S.A. wrote the first draft of the paper and all the authors edited the paper.

Competing Interests

All authors declare they have no competing interests.

Acknowledgments

Extended Data

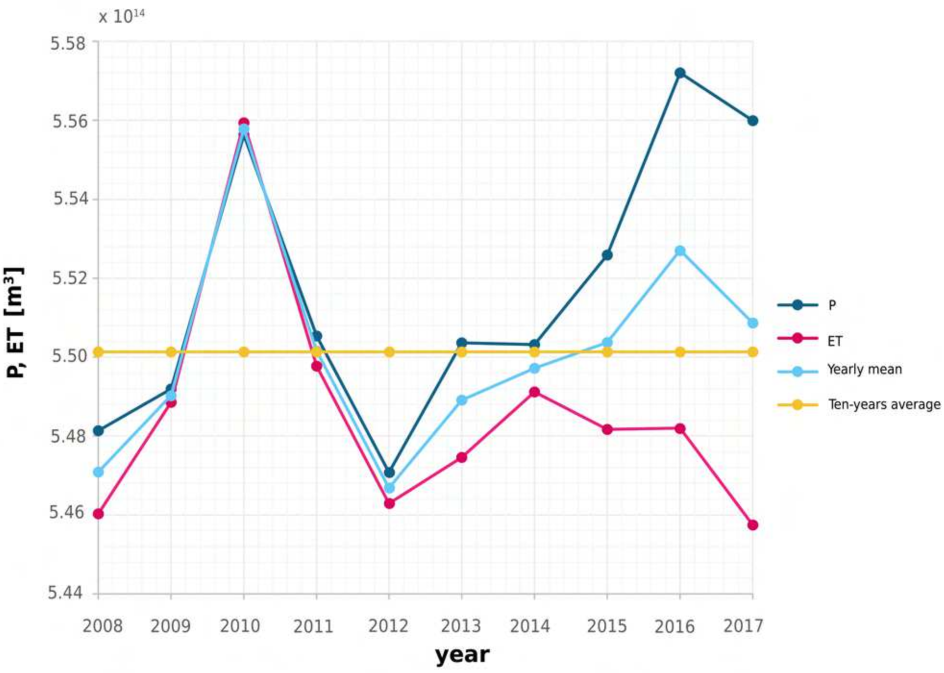

Extended Data Figure 1 Ten-years time series (2008-2017) of ERA5 total precipitation (P, blue line) and evaporation (ET, magenta line) at the global scale. The light-blue line represents the yearly mean between $P(y)$ and $ET(y)$, while the yellow line is the ten-year average between P and ET.

Extended Data Table 1 Ten-years (2008-2017) annual volumes of ERA5 total precipitation (P) and evaporation (ET), their ratio (precipitation over evaporation) and their relative percentage difference $d_{rel}(y)$ [%]

Year	***P*** $[10^5$ km$^3]$	***ET*** $[10^5$ km$^3]$	***P/ET*** [-]	$d_{rel}(y)$ [%]
2008	5.48	5.46	1.004	-0.4
2009	5.49	5.48	1.001	-0.2
2010	5.55	5.56	0.999	0.2
2011	5.51	5.50	1.001	-0.2
2012	5.47	5.46	1.001	-0.2
2013	5.50	5.47	1.005	-0.54
2014	5.50	5.49	1.002	-0.18
2015	5.53	5.48	1.008	-0.9
2016	5.57	5.48	1.016	-1.7
2017	5.56	5.46	1.019	-1.8

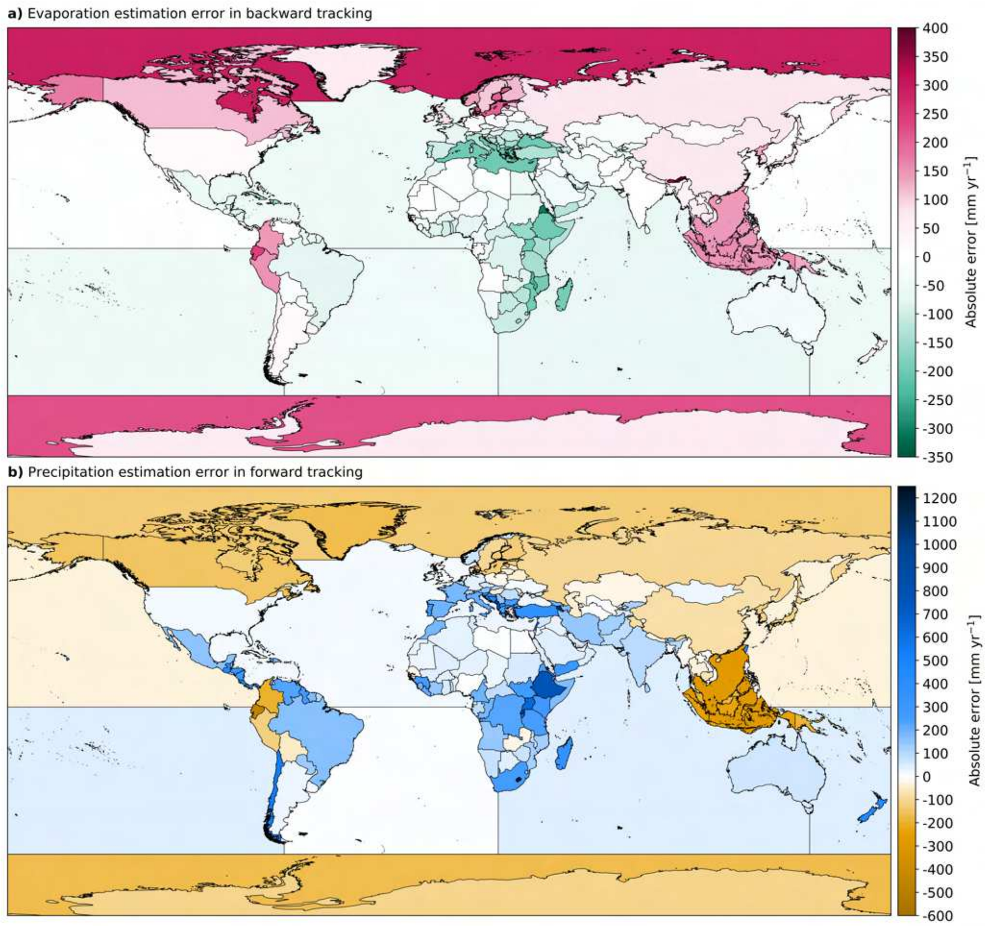

Extended Data Figure 2 Absolute deviations [mm · yr^{-1}] between ERA5 data and the UTrack estimates at country/ocean scale, referred to the average year in the interval [2008-2017]. Comparison between ERA5 reanalysis and **(a)** evaporation estimated by backward approach and **(b)** precipitation estimates obtained by forward approach.

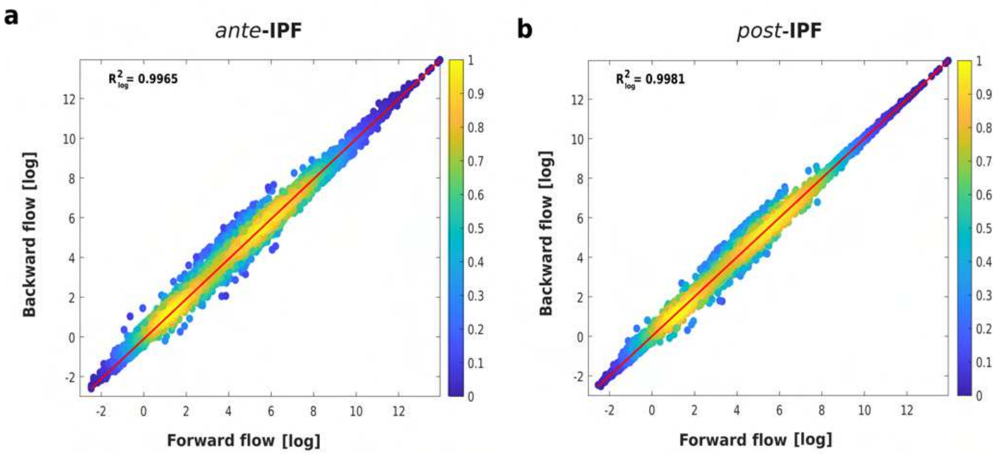

Extended Data Figure 3 Comparison of bilateral flows between the forward and backward matrices at the country/ocean scale sourced from the UTrack dataset *ante*- and *post*- Iterative Proportional Fitting (IPF) application. **(a)** density scatter plot of bilateral moisture volumes forward-reconstructed (on the x-axis) and backward-reconstructed (on the y-axis) **(a)** *ante*- and **(b)** *post*-IPF application (values are plotted in logarithmic scale). R squared values in the two cases show the increased fitting to the one-one line achieved with the IPF application.

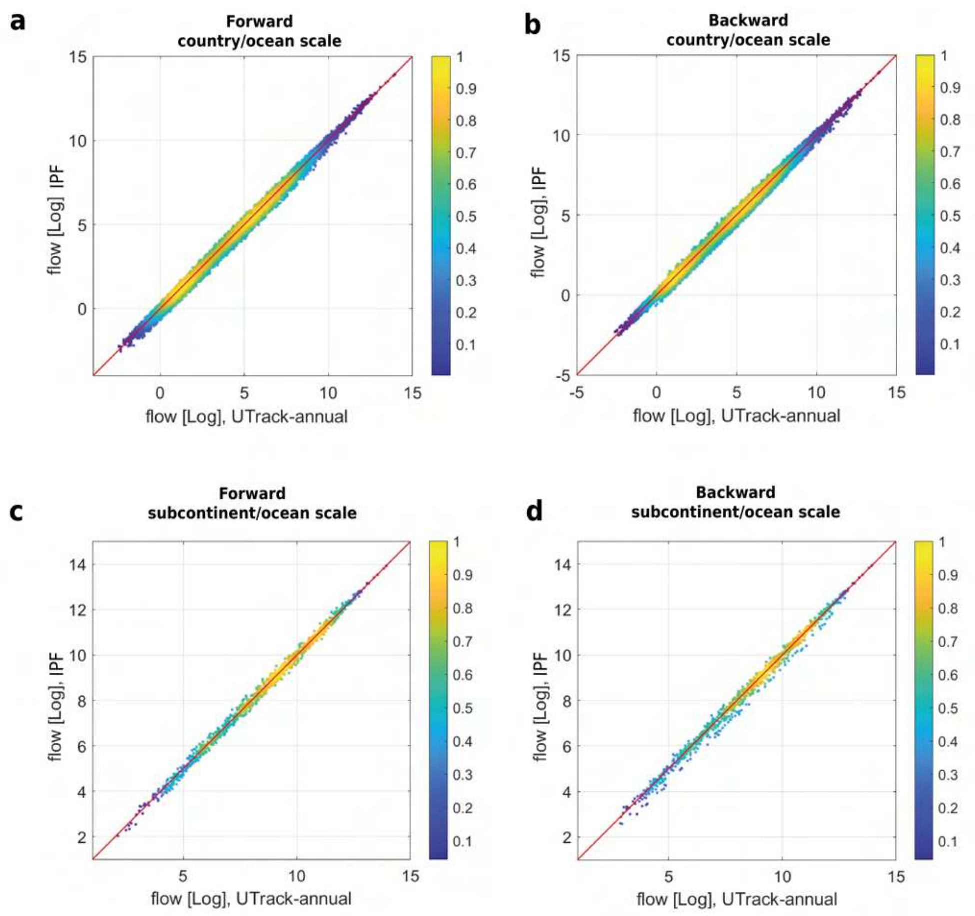

Extended Data Figure 4 Comparison of bilateral flow changes *ante-* and *post-*Iterative Proportional Fitting (IPF) application for the forward and backward matrices of atmospheric moisture connections at the country/ocean scale and subcontinental/ocean scale sourced from the UTrack dataset. **(a), (b)** density scatter plot of bilateral moisture volumes at the country/ocean scale before (on the x-axis) and after (on the y-axis) the IPF application (values are plotted in logarithmic scale) in the forward and backward case, respectively. **(c), (d)** density scatter plot of bilateral moisture volumes at the subcontinent/ocean scale before (on the x-axis) and after (on the y-axis) the IPF application (values are plotted in logarithmic scale) in the forward and backward case, respectively.

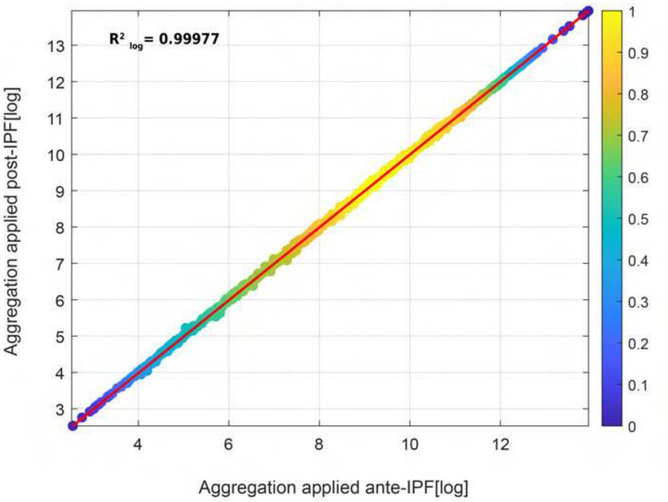

Extended Data Figure 5 Density scatter plot of bilateral flow *post*-Iterative Proportional Fitting (IPF) application for the composite matrix of forward and backward atmospheric moisture connections sourced from the UTrack dataset in the case (on the x-axis) of a region/ocean matrix aggregated before the IPF application and (on the y-axis) after the IPF application to a country/ocean matrix (values are plotted in logarithmic scale).

Extended Data Table 2 Comparison of major and minor country-specific terrestrial moisture recycling (TMR) *ante*- and *post*-Iterative Proportional Fitting (IPF). The table presents the percentage values of *ante*-IPF (TMR_{UTrack}) and *post*-IPF ($TMR_{UTrack_{(IPF)}}$) for selected countries with the highest and lowest TMR. Small island states are not reported in this table.

Country	TMR_{UTrack} [%] *ante*-IPF	$TMR_{UTrack_{(IPF)}}$ [%] *post*-IPF
Mongolia	97	95
CAR	84	88
Congo	84	87
Chad	84	87
Kyrgyzstan	87	85
Cameroon	79	83
Sudan	80	84
Gabon	78	82
Paraguay	79	79
Tajikistan	79	79
United Kingdom	18	16
Nicaragua	15	15
Guyana	12	13
Iceland	16	13
Ireland	14	11
New Zealand	12	12
Suriname	11	11
Portugal	9	9
French Guiana	7	7
Chile	4	4

Extended Data Table 3 Subcontinental annual precipitation and evaporation flows [km^3] and subcontinental annual precipitation and evaporation flows per area (*Area*), [m]. Net precipitation (*NetP*) is the absolute difference between annual precipitation and evaporation, expressed both as a difference in volume difference [km^3] and in volume per unit of surface area [m], when referred to the area *Area* of the subcontinent or ocean. Values refer to the average year between 2008 and 2017.

Subcontinent/Ocean	***P*** [km^3]	***ET*** [km^3]	***Net P*** [km^3]	***P/Area*** [m]	***ET/Area*** [m]	***Net P/Area*** [m]
Antarctica	$3.17 \cdot 10^3$	$4.05 \cdot 10^2$	$2.77 \cdot 10^3$	0.2	0.0	0.2
Arctic Ocean	$6.24 \cdot 10^3$	$3.57 \cdot 10^3$	$2.67 \cdot 10^3$	0.5	0.3	0.2
Australia and New Zealand	$5.39 \cdot 10^3$	$5.92 \cdot 10^3$	$-5.28 \cdot 10^2$	11	12	-1.1
Caspian Sea	$7.79 \cdot 10^1$	$2.85 \cdot 10^2$	$-2.07 \cdot 10^2$	0.3	1.1	-0.8
Central Africa	$6.72 \cdot 10^3$	$5.73 \cdot 10^3$	$9.94 \cdot 10^2$	5	4.0	0.7
Central America	$4.60 \cdot 10^3$	$4.04 \cdot 10^3$	$5.64 \cdot 10^2$	508	446	62
Central Asia	$1.30 \cdot 10^3$	$1.43 \cdot 10^3$	$-1.33 \cdot 10^2$	2.2	2.4	-0.2
Eastern Africa	$7.20 \cdot 10^3$	$6.79 \cdot 10^3$	$4.10 \cdot 10^2$	490	462	28
Eastern Asia	$1.09 \cdot 10^4$	$7.18 \cdot 10^3$	$3.72 \cdot 10^3$	124	82	42
Eastern Europe	$1.20 \cdot 10^4$	$7.52 \cdot 10^3$	$4.45 \cdot 10^3$	136	85	50
Indian Ocean	$7.98 \cdot 10^4$	$9.87 \cdot 10^4$	$-1.89 \cdot 10^4$	1.2	1.4	-0.3
Mediterranean Sea	$9.27 \cdot 10^2$	$2.50 \cdot 10^3$	$-1.57 \cdot 10^3$	0.5	1.2	-0.8
Melanesia	$5.34 \cdot 10^3$	$2.33 \cdot 10^3$	$3.01 \cdot 10^3$	50	22	28
Micronesia	$1.26 \cdot 10^3$	$9.51 \cdot 10^2$	$3.08 \cdot 10^2$	35	26	9
North Atlantic Ocean	$4.67 \cdot 10^4$	$5.90 \cdot 10^4$	$-1.24 \cdot 10^4$	1.2	1.5	-0.3
North Pacific Ocean	$1.16 \cdot 10^5$	$1.09 \cdot 10^5$	$7.74 \cdot 10^3$	1.6	1.5	0.1
Northern Africa	$7.69 \cdot 10^2$	$1.20 \cdot 10^3$	$-4.31 \cdot 10^2$	45	70	-25
Northern America	$1.79 \cdot 10^4$	$1.00 \cdot 10^4$	$7.92 \cdot 10^3$	9	4.9	4
Northern Europe	$2.45 \cdot 10^3$	$1.16 \cdot 10^3$	$1.29 \cdot 10^3$	6	2.8	3
Polynesia	$1.03 \cdot 10^3$	$1.24 \cdot 10^3$	$-2.10 \cdot 10^2$	12	14	-2
South America	$3.27 \cdot 10^4$	$1.95 \cdot 10^4$	$1.32 \cdot 10^4$	260	155	105
South Atlantic Ocean	$3.17 \cdot 10^4$	$4.92 \cdot 10^4$	$-1.75 \cdot 10^4$	0.8	1.2	-0.4
South China & Easter Arch. Seas	$1.06 \cdot 10^4$	$7.08 \cdot 10^3$	$3.55 \cdot 10^3$	2.2	1.5	0.7
South Pacific Ocean	$9.44 \cdot 10^4$	$1.17 \cdot 10^5$	$-2.25 \cdot 10^4$	1.1	1.4	-0.3
South-eastern Asia	$1.85 \cdot 10^4$	$9.09 \cdot 10^3$	$9.38 \cdot 10^3$	3310	1628	1682
Southern Africa	$1.44 \cdot 10^3$	$1.47 \cdot 10^3$	$-2.92 \cdot 10^1$	1	1.02	-0.02
Southern Asia	$6.45 \cdot 10^3$	$4.81 \cdot 10^3$	$1.63 \cdot 10^3$	31.5	23	8
Southern Europe	$1.56 \cdot 10^3$	$1.63 \cdot 10^3$	$-6.98 \cdot 10^1$	672	702	-30
Southern Ocean	$1.53 \cdot 10^4$	$5.49 \cdot 10^3$	$9.77 \cdot 10^3$	0.7	0.3	0.5
Western Africa	$5.02 \cdot 10^3$	$3.82 \cdot 10^3$	$1.20 \cdot 10^3$	268	204	64
Western Asia	$1.10 \cdot 10^3$	$1.58 \cdot 10^3$	$-4.73 \cdot 10^2$	1.8	2.6	-0.8
Western Europe	$1.14 \cdot 10^3$	$7.43 \cdot 10^2$	$3.94 \cdot 10^2$	16	10	5
	$1.4 \cdot 10^3$	$1.5 \cdot 10^3$	$7.1 \cdot 10^1$	2	2	0

Extended Data Table 4 Major ten annual volumes of atmospheric moisture flows between terrestrial sources and sinks at the subcontinental scale ([km^3]).

Source	**Sink**	**Volume [km^3]**
Eastern Africa	Central Africa	$1.67 \cdot 10^3$
Southern Asia	Eastern Asia	$1.12 \cdot 10^3$
Southeast Asia	Eastern Asia	$9.81 \cdot 10^2$
Central Africa	Western Africa	$9.58 \cdot 10^2$
Central America	Northern America	$8.11 \cdot 10^2$
Eastern Asia	Eastern Europe	$6.24 \cdot 10^2$
Central Asia	Eastern Europe	$5.87 \cdot 10^2$
Australia and New Zealand	Southeast Asia	$4.50 \cdot 10^2$
Southern Europe	Eastern Europe	$4.36 \cdot 10^2$
Southern Asia	Southeast Asia	$4.12 \cdot 10^2$

Extended Data Table 5 Precipitation volumes originated from terrestrial evaporation (P_{terr}) and evaporation precipitating on other lands (ET_{terr}) at the subcontinent scale. The flag indicates whether the region is a net importer or exporter of terrestrial atmospheric moisture flow and to which degree [%]. The degree of net import (or net export) is calculated as the ratio between the net flow and the total import (or total export) from (or to) other terrestrial regions. The terrestrial moisture recycling ratio (TMR) for each subcontinental region indicates the weight of precipitation from terrestrial sources over the total precipitation from both oceanic and terrestrial evaporation volumes.

Subcontinent	P_{terr} [km^3]	ET_{terr} [km^3]	**TMR** [%]	**Flag**	**Degree** [%]
Australia and New Zealand	$1.65 \cdot 10^3$	$2.12 \cdot 10^3$	31	net exporter	8
Central Africa	$5.31 \cdot 10^3$	$4.71 \cdot 10^3$	79	net importer	9
Central America	$1.20 \cdot 10^3$	$1.79 \cdot 10^3$	26	net exporter	14
Central Asia	$9.60 \cdot 10^2$	$1.37 \cdot 10^3$	74	net exporter	28
Eastern Africa	$3.35 \cdot 10^3$	$5.29 \cdot 10^3$	46	net exporter	29
Eastern Asia	$6.94 \cdot 10^3$	$4.94 \cdot 10^3$	64	net importer	18
Eastern Europe	$7.89 \cdot 10^3$	$6.04 \cdot 10^3$	66	net importer	15
Melanesia	$9.80 \cdot 10^2$	$9.75 \cdot 10^2$	18	net importer	0
Micronesia	$5.41 \cdot 10^1$	$1.08 \cdot 10^2$	4	net exporter	6
Northern Africa	$4.47 \cdot 10^2$	$9.62 \cdot 10^2$	58	net exporter	43
Northern America	$7.61 \cdot 10^3$	$6.84 \cdot 10^3$	42	net importer	4
Northern Europe	$6.55 \cdot 10^2$	$7.51 \cdot 10^2$	27	net exporter	8
Polynesia	$5.00 \cdot 10^1$	$9.35 \cdot 10^1$	5	net exporter	4
South America	$1.47 \cdot 10^4$	$1.46 \cdot 10^4$	45	net importer	0
South-eastern Asia	$5.14 \cdot 10^3$	$4.97 \cdot 10^3$	28	net importer	1
Southern Africa	$8.16 \cdot 10^2$	$6.58 \cdot 10^2$	57	net importer	11
Southern Asia	$2.71 \cdot 10^3$	$3.53 \cdot 10^3$	42	net exporter	17
Southern Europe	$5.52 \cdot 10^2$	$1.25 \cdot 10^3$	35	net exporter	43
Western Africa	$3.16 \cdot 10^3$	$2.16 \cdot 10^3$	63	net importer	20
Western Asia	$5.65 \cdot 10^2$	$1.39 \cdot 10^3$	51	net exporter	52
Western Europe	$3.60 \cdot 10^2$	$5.93 \cdot 10^2$	32	net exporter	31

References

[1] IPCC: Climate change 2021: The physical science basis. contribution of working group i to the sixth assessment report of the intergovernmental panel on climate change. Cambridge University Press (2021)

[2] Rudebeck, T., Schmuhl: Corporations as custodians of the public good? Cham, Switzerland: Springer International Publishing (2019)

[3] Xu, L., Mao, F., Famiglietti, J.S., Pomeroy, J.W., Pahl-Wostl, C.: Conceptualizing cascading effects of resilience in human–water systems. Multisystemic resilience: Adaptation and transformation in contexts of change, 744–767 (2021)

[4] Dirmeyer, P.A., Brubaker, K.L., DelSole, T.: Import and export of atmospheric water vapor between nations. Journal of Hydrology **365**, 11–22 (2009) https://doi.org/10.1016/j.jhydrol.2008.11.016

[5] Dirmeyer, P.A., Brubaker, K.L.: Contrasting evaporative moisture sources during the drought of 1988 and the flood of 1993. Journal of Geophysical Research: Atmospheres **104**(D16), 19383–19397 (1999)

[6] Brubaker, K.L., Dirmeyer, P.A., Sudradjat, A., Levy, B.S., Bernal, F.: A 36-yr climatological description of the evaporative sources of warm-season precipitation in the mississippi river basin. Journal of Hydrometeorology **2**(6), 537–557 (2001)

[7] Xie, P., Arkin, P.A.: Global precipitation: A 17-year monthly analysis based on gauge observations, satellite estimates, and numerical model outputs. Bulletin of the American Meteorological Society **78**, 2539–2558 (1997) https://doi.org/10.1175/1520-0477(1997)078⟨2539:GPAYMA⟩2.0.CO;2

[8] Kanamitsu, M., Ebisuzaki, W., Woollen, J., Yang, S.-K., Hnilo, J.J., Fiorino, M., Potter, G.L.: Ncep–doe amip-ii reanalysis (r-2). Bulletin of the American Meteorological Society **83**, 1631–1644 (2002) https://doi.org/10.1175/BAMS-83-11-1631

[9] Keys, P.W., Wang-Erlandsson, L., Gordon, L.J., Galaz, V., Ebbesson, J.: Approaching moisture recycling governance. Global Environmental Change **45**, 15–23 (2017)

[10] Link, A., Ent, R., Berger, M., Eisner, S., Finkbeiner, M.: The fate of land evaporation – a global dataset. Earth System Science Data **12**, 1897–1912 (2020) https://doi.org/10.5194/essd-12-1897-2020

[11] Tuinenburg, O.A., Staal, A.: Tracking the global flows of atmospheric moisture and associated uncertainties. Hydrology and Earth System Sciences **24**(5), 2419–2435 (2020)

[12] Tuinenburg, O.A., Theeuwen, J.J., Staal, A.: High-resolution global atmospheric moisture connections from evaporation to precipitation. Earth System Science

Data **12**(4), 3177–3188 (2020)

[13] Pukelsheim, F.: Biproportional scaling of matrices and the iterative proportional fitting procedure. Annals of Operations Research **215**, 269–283 (2014)

[14] Distefano, T., Tuninetti, M., Laio, F., Ridolfi, L.: Tools for reconstructing the bilateral trade network: a critical assessment. Economic Systems Research **32**, 378–394 (2020) https://doi.org/10.1080/09535314.2019.1703173

[15] Hersbach, H., Bell, B., Berrisford, P., Hirahara, S., Horányi, A., Muñoz-Sabater, J., Nicolas, J., Peubey, C., Radu, R., Schepers, D., *et al.*: The era5 global reanalysis. Quarterly Journal of the Royal Meteorological Society **146**(730), 1999–2049 (2020)

[16] Ruschendorf, L.: Convergence of the iterative proportional fitting procedure. The Annals of Statistics, 1160–1174 (1995)

[17] Bosilovich, M.G., Robertson, F.R., Takacs, L., Molod, A., Mocko, D.: Atmospheric water balance and variability in the merra-2 reanalysis. Journal of Climate **30**, 1177–1196 (2017) https://doi.org/10.1175/JCLI-D-16-0338.1

[18] Lehmann, F., Vishwakarma, B.D., Bamber, J.: How well are we able to close the water budget at the global scale? Hydrology and Earth System Sciences **26**, 35–54 (2022) https://doi.org/10.5194/hess-26-35-2022

[19] Hobeichi, S., Abramowitz, G., Ukkola, A.M., De Kauwe, M., Pitman, A., Evans, J.P., Beck, H.: Reconciling historical changes in the hydrological cycle over land. npj Climate and Atmospheric Science **5**(1), 17 (2022)

[20] Ent, R.J.: Origin and fate of atmospheric moisture over continents. Water Resources Research **46** (2010) https://doi.org/10.1029/2010WR009127

[21] Posada-Marín, J.A., Arias, P.A., Jaramillo, F., Salazar, J.F.: Global impacts of el niño on terrestrial moisture recycling. Geophysical Research Letters **50** (2023) https://doi.org/10.1029/2023GL103147

[22] Fahrländer, S.F., Wang-Erlandsson, L., Pranindita, A., Jaramillo, F.: Hydroclimatic vulnerability of wetlands to upwind land use changes. Earth's Future **12** (2024) https://doi.org/10.1029/2023EF003837

[23] Wang, Y., Liu, X., Zhang, D., Bai, P.: Tracking moisture sources of precipitation over china. Journal of Geophysical Research: Atmospheres **128** (2023) https://doi.org/10.1029/2023JD039106

[24] O'Connor, J.C., Santos, M.J., Dekker, S.C., Rebel, K.T., Tuinenburg, O.A.: Atmospheric moisture contribution to the growing season in the amazon arc of deforestation. Environmental Research Letters **16**, 084026 (2021) https://doi.org/

10.1088/1748-9326/ac12f0

[25] Wierik, S.A., Gupta, J., Cammeraat, E.L., Artzy-Randrup, Y.A.: The need for green and atmospheric water governance. Wiley Interdisciplinary Reviews: Water **7**(2), 1406 (2020)

[26] Benedict, I., Weijenborg, C., Keune, J.: Moisture tracking community meeting - spm3 at egu23. EGU General Assembly 2023 (2023)

[27] Keys, P.W., Wang-Erlandsson, L.: On the social dynamics of moisture recycling. Earth System Dynamics **9**(2), 829–847 (2018)

[28] Keys, P.W., Porkka, M., Wang-Erlandsson, L., Fetzer, I., Gleeson, T., Gordon, L.J.: Invisible water security: Moisture recycling and water resilience. Water Security **8**, 100046 (2019)

[29] Keys, P.W., Wang-Erlandsson, L., Moore, M.-L., Pranindita, A., Stenzel, F., Varis, O., Warrier, R., Wong, R.B., D'Odorico, P., Folke, C.: The dry sky: future scenarios for humanity's modification of the atmospheric water cycle. Global Sustainability **7**, 11 (2024) https://doi.org/10.1017/sus.2024.9

[30] Allan, J.A.: Virtual water-the water, food, and trade nexus. useful concept or misleading metaphor? Water international **28**(1), 106–113 (2003)

[31] Schulzweida, U., Kornblueh, L., Quast, R.: CDO user guide (2019)

[32] Tuinenburg, O.A. https://github.com/ObbeTuinenburg/UTrack_global_database (2020)

[33] GISCO., E.C.E.E.: Countries, 2020 - Administrative Units - Dataset ID 5C27B6C0-BC1C-4175-9B0B-783AEEBAAD61 (2020). https://ec.europa.eu/eurostat/web/gisco/geodata/reference-data/administrative-unitsstatistical-units/countries

[34] Institute, F.M.: Global Oceans and Seas, version 1. Available online at https://www.marineregions.org/. (2021). https://doi.org/10.14284/542. . https://www.marineregions.org/download_file.php?name=GOaS_v1_20211214.zip

[35] (BODC), U.K.B.O.D.C.: Polygon dataset of the extent of water bodies from the SeaVoX Salt and Fresh Water Body Gazetteer (v19), Available online at https://www.marineregions.org/ (2023). https://doi.org/10.14284/590 . https://www.marineregions.org/sources.php#seavox

[36] contributors, G.: GDAL/OGR Geospatial Data Abstraction software Library. Open Source Geospatial Foundation (2022). https://doi.org/10.5281/zenodo.5884351 . https://gdal.org

[37] (UNSD), U.N.S.D.: Standard Country or Area Codes for Statistical Use, Available online at https://unstats.un.org/unsd/methodology/m49/ (2023). https://doi.org/10.14284/590 . https://unstats.un.org/unsd/methodology/m49/